Nanoscale

Accepted Manuscript

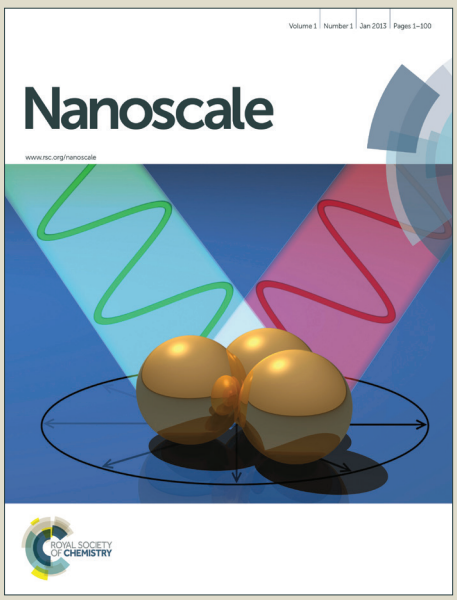

ROYAL SOCIETY OF CHEMISTRY

www.rsc.org/nanoscale

Journal Name

RSCPublishing

COMMUNICATION

Local defect-induced red-shift of cathodoluminescence in individual ZnS nanobelt

Cite this: DOI: 10.1039/x0xx00000x

B. D. Liu,[a,*] B. Yang,[a] B. Dierre,[b] T. Sekiguchi,[b] and X. Jiang[a,*]

Received 00th January 2014,
Accepted 00th January 2014

DOI: 10.1039/x0xx00000x

www.rsc.org/

The luminescence of semiconductor nanostructures is strongly dependent on their size, dimension, morphology, composition, or defects, and their band emissions can be properly and selectively tailored through the rational manipulation of these parameters during material growth. Using spatially-resolved cathodoluminescence spectroscopy, monochromatic contrast maps and high-resolution transmission electron microscopy, an obvious red-shift of the near-band-edge emission of wurtzite ZnS nanobelts, resulting from a strip of stacking faults or zinc-blende phase with tens of atomic layers in width, has been observed and its related mechanism has been discussed. This finding is not specific to the defect-dependent optical properties tailoring of ZnS nanostructures and represents a general validity for clarifying the mechanism of peak-shift (band-gap expansion or shrinking) of a wide range of semiconductor nanostructures with various defects. In addition, the general formation mechanism of belt-like nanostructure was proposed based on precise microstructure analyses on ZnS nanobelt with atomic terrace growth fronts.

Introduction

ZnS nanostructures with diverse morphologies are ideal fundamental building blocks for the integration of nano-scaled optoelectronic devices, ranging from UV-photodetector and chemical sensors to field-emission display (FED) and light emitting diode (LED), due to their wide-band-gap, fast/sensitive response to UV irradiation and reactive gases, and excellent opto-electronic property.[1-7] Generally, ZnS-based nanodevices with excellent performance require a good crystallinity and rather high phase purity since a direct band-to-band transition will contribute to higher quantum conversion efficiency. In some cases, the flatness and smoothness of ZnS nanostructures with a featured belt-like morphology are also expected for harvesting more light absorption in ZnS-based optoelectronic photodetectors.[1, 8] However, the intrinsic and direct band-to-band transition in ZnS nanostructures is rarely observed due to the challenge of pure and defect-free material,[1, 2] and ZnS nanostructures synthesized from different routines such as chemical vapor deposition (CVD) process[8] and hydrogen thermal growth[9] will contain more or less defects, i.e., structural defects like various point defects (Zn and S vacancies), line defects (threading dislocations), plane defects (stacking faults and twinned structures),[8, 10] as well as impurity-related composition inhomogeneity and phase separation.[3] All these defects, either structural or compositional ones, will give rise to some defect-related energy levels in either beneath of the conduction band or the top of valance band, leading to obvious defect-related optical emissions.[10] Our previous study on T-shaped ZnS nanostructures has demonstrated that crystal domain boundary and twin defect could induce a strong visible emission in the range of 400-1000 nm.[10] However, it is rather difficult and challenging to evaluate the influence of these local defects on the inter-band emission in single ZnS nanobelt, especially, when the size of ZnS nanostructures falls into nano-scale and the defect area only covers a strip of several atomic layers in width. To directly understand the inner mechanism of these defect-related emissions, it requires ideal target nanostructure containing clearly identified structural defects. However, the critical size and random distribution of defects in previous ZnS nanostructures make such a highly-resolved defect-dependent optical investigation quite challenging, and it is difficult to locate the exact position of these structural defects during optical analysis. Fortunately, ZnS nanobelts synthesized in this work provide ideal target samples for performing in-situ defect-related cathodoluminescence (CL) study and this enables us to fully understand the origin of optical emission shift, as well as the correlation between structural defects and CL emission behavior. Indeed, the availability of ZnS nanobelts with featured defect would be also extremely interesting and intriguing in the design and fabrication of ZnS-based optoelectronic nanodevices. This work also presents a direct evidence to elucidate the defect-induced peak shifting in ZnS nanostructures.

Experimental section

Nanobelt synthesis

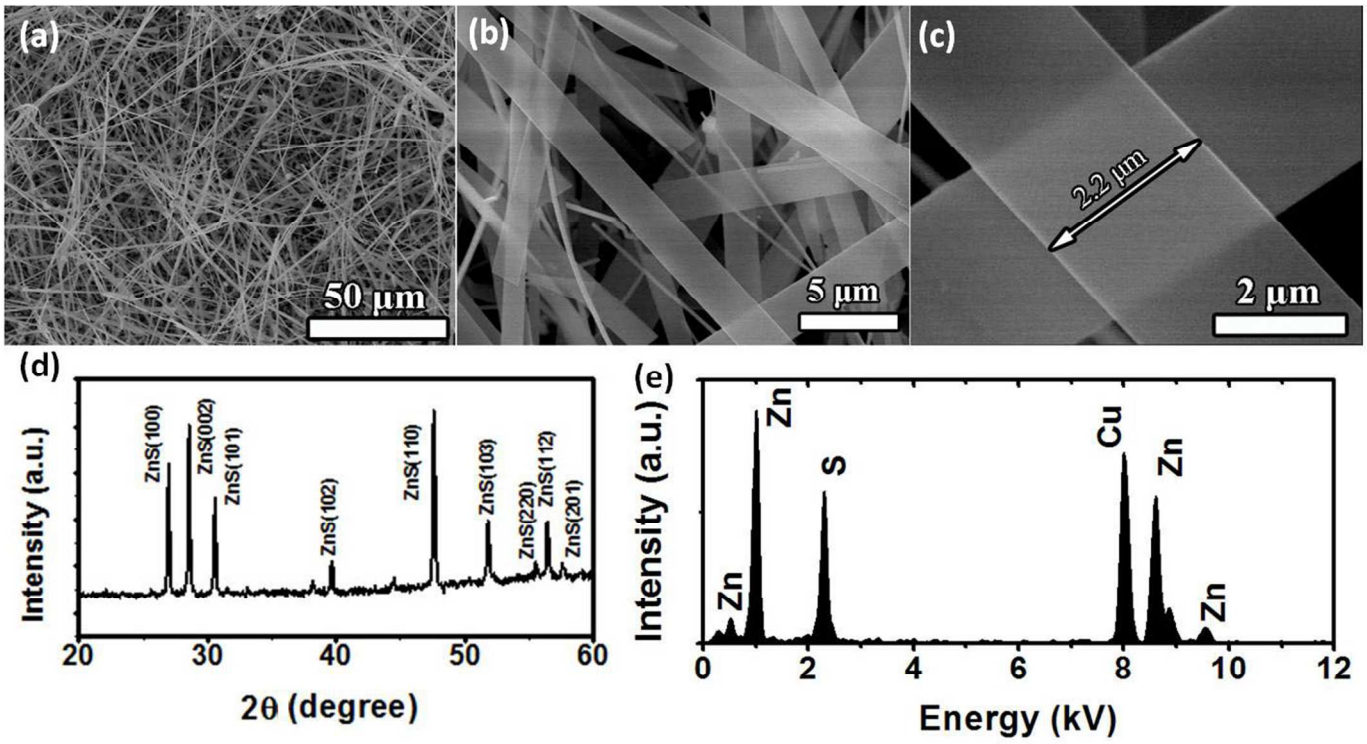

Figure 1 (a-c) SEM images showing general features of ZnS nanobelts under different magnifications; (d) XRD pattern of ZnS nanobelts deposited on Si substrate in the range of 20-60 degrees; (e) representative compositional spectrum of ZnS nanobelts using EDS.

ZnS nanobelts with strip of structural defect were obtained through a simple CVD process, as reported elsewhere.[8] Typically, ZnS powders loaded into an Al_2O_3 crucible were used as precursors and inserted into the centre of a quartz-tube. Si substrate coated with a thin Au layer was placed on the downstream area close to the gas outlet. The reaction chamber was then quickly heated to 1100^{o}C under an Ar flow (100 mL/min). After reacting at this temperature for 30 min, large amount of fiber-like ZnS microbelts were found deposited on the Si substrate.

Morphology and structure characterization

The phase, morphology, crystallinity and composition of ZnS nanobelts were studied by means of an X-ray powder diffractometer (XRD, Rigaku RINT 2000) operating at 40 kV and 40 mA by using Cu K_α radiation (λ=1.54056 Å), a scanning electron microscope [(SEM) JEOL, JSM-6700F], and a high-resolution field-emission transmission electron microscope [(TEM) FEI, Tecnai G2 F20] equipped with an X-ray energy dispersive spectrometer (EDS).

Cathodoluminescence characterization

The CL spectra of ZnS nanobelts and their spatially-resolved CL images were taken in a field emission SEM (Hitachi, S4300) equipped with a CL system (Horiba, MP32S/M). The applied voltage and beam current in this work are 5 kV and 2000 pA, respectively. To characterize local spatially-resolved cathodoluminescence, individual ZnS nanobelt suspending on TEM grid is used. Details for the measurement can be found in previous work.[11]

Results and discussion

ZnS nanobelts with smooth surface were achieved via a simple thermal evaporation process, as previously reported elsewhere.[8] Typically, high purity ZnS powers with a size of micro-order were used as the precursor for the formation of ZnS nanobelts through a simple CVD reaction at a temperature as high as 1100 ^{o}C in the protection of flowing Ar gas. Fig. 1a-1c shows SEM images of ZnS nanostructures densely covered on Si substrate. It can be seen that the majorities of the products are featured as flat and smooth ZnS nanobelts with an average length estimated to be more than several hundreds of μm (Figure 1a) and a typical belt thickness of 20~50 nm. A slight fraction of ZnS nanowires can also be found in the fiber-like products. These ZnS nanobelts exhibit a typical size of 2-5 micrometers in width and a very small thickness (~20 nm), which enables them a transparent appearance and allows the electrons easily penetrating into their lattice during CL measurement (Figure 1b-1c). The flatness, width and large surface-to-volume ratio of ZnS nanobelts offer them many advantages in optical absorption and make them as ideal candidates for sensitive photodetection.[1] XRD measurement, scanning from 20 to 60 degrees, confirmed that all the diffraction peaks excluding the ones from Au catalysts can be properly assigned to standard wurtzite-type ZnS phase, while metastable cubic zinc-blende-type ZnS phase was not detected within the resolution of XRD (Fig. 1d). Chemical composition analysis performed on tens of ZnS nanobelts concluded that the nanobelts are only made of Zn and S elements with a stoichiometric ratio approaching to standard ZnS crystal (Figure 1e), implying the high chemical purity of ZnS nanobelts. In addition, the ZnS nanobelts also show decent reproducibility under current growth conditions.

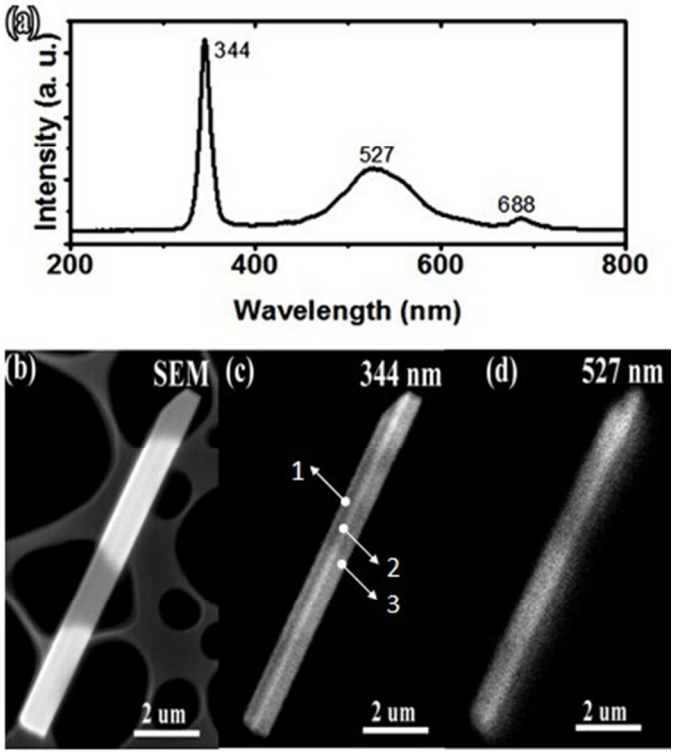

Figure 2 (a) CL spectrum recorded from large amount of ZnS nanobelts under an accelerated voltage of 5 kV and a beam current of 2000 pA; (b) SEM image of a single ZnS nanobelt with smooth morphology surface and dangling on TEM grid for accurate CL characterization; (c, d) CL mapping of the ZnS nanobelt detecting emissions at 344 nm and 527 nm, respectively.

As a key luminescent material, ZnS crystal free of defect shows an intrinsic band-gap emission at the wavelength of 329 nm (corresponding to a band-gap of 3.77 eV) for hexagonal wurtzite-type phase[12] and 333 nm (corresponding to a band-gap of 3.72 eV) for cubic zinc-blende-type phase,[13] respectively. However, the achievement of direct band-gap emission of pure ZnS structures is quite challenging due to unintentional impurity doping and/or the generation of structural defect during their nucleation and subsequent crystallization. Wide range emissions from ultraviolet to visible light have been observed in various ZnS structures in either bulk or nano-size.[1, 2, 10, 14-16] To investigate the optical characteristic of ZnS nanobelts, spatially-resolved CL spectroscopy is used. Figure 2a shows a typical CL curve taken under an accelerated voltage of 5 kV and a beam current of 2000 pA. Two main emission bands with different CL intensities can be found in the range of 200-800 nm (The 688 nm emission band corresponds to the second order of the 344 nm emission). The sharp peak centered at 344 nm, which can be assigned to the near-band-edge emission (NBE) of hexagonal WZ-ZnS phase, exhibited predominant luminescence intensity with a full width of half maximum (FWHM) value of ~13 nm. The narrow peak and small FWHM value indicate the superior optical property of ZnS nanobelts. Although the 344-nm emission peak slightly deviates from the reported data concerning intrinsic band-to-band emission,[17] it is still consistent with the observed UV-emissions for hexagonal ZnS phase.[18, 19] The origin of the broad band in the visible range (~527 nm) is rather complex and is still in debate.[20-22] It has been reported that structural defects such as S/Zn vacancies can cause the

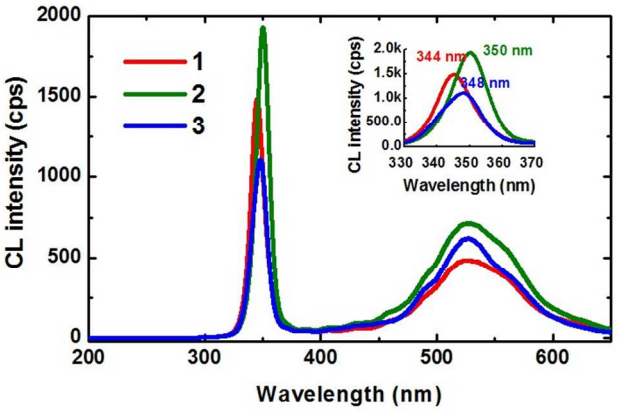

Figure 3 High-resolution CL spectra recorded from different regions of a single ZnS nanobelt shown in Figure 2c using point mode. The inset in right-up is the magnified CL curves in UV range, reflecting the precise CL peak difference of different nano-scaled areas inside of an individual ZnS nanobelt shown in Figure 2b.

blue emission.[18] In order to precisely determine the spatial luminescence regions responsible for the NBE and broad visible emission, high-resolution CL monochromatic imaging was carried out.[23, 24] Figure 2b shows a flat ZnS nanobelt with smooth surface and its corresponding CL images recorded at 344-nm and 527-nm were also presented in Fig. 2c and 2d, respectively. Interestingly, the 344-nm luminescence image consists of two distinct regions: one bright strip with a width of 200 nm along the growth direction and the other areas on the belt edges, as marked in Fig. 2c, whereas the ZnS nanobelt itself shows no difference in morphology. It can be seen that the luminescence intensity in either of the two areas is quite uniform. The 527-nm CL image, shown in Fig. 2d, mainly arises from the left side of the nanobelt and shows an inhomogeneous intensity distribution.

The investigation of the spatial CL imaging and the distinct luminescence intensity difference within an individual ZnS nanobelt promote us to make more accurate optical study on the different areas. To elucidate the optical behavior of different regions, CL spectra collecting in point mode were performed from one side to the other side of ZnS nanobelt along the lateral direction in order to ensure the luminescence difference can be clearly distinguished. With this purpose, three points with a given distance were selected, i.e., the first one on the left edge, the second one on the strip area in the 344-nm CL image and the last one on the right side of the ZnS nanobelt, as presented in Fig. 2d. The electron beam size is set smaller enough (~few tens nm) to allow the electrons injecting into the local investigated area. The spectra collected from the three different areas were plotted in Fig. 3. One can clearly see again that all the spectra show a strong UV emission and a broad visible emission. For the visible emission band, all the three curves collected from areas 1, 2 and 3 exhibit no obvious difference (peak shift) in spite of the peak intensity. On the other hand, the three peaks in UV range, which were recorded from three distinct areas, not only exhibit difference in peak intensity, but also show obvious peak shift, as presented in the magnified curves in inset. The CL spectrum collected from the left side (read curve, area "1") of the ZnS nanobelt possesses a medium intensity and the shortest wavelength of 344 nm. Similarly, the right side of the belt (blue curve, area "3") shows a sharp peak centred at 348 nm. Compared with the two edge emissions, the CL spectrum arising from the strip

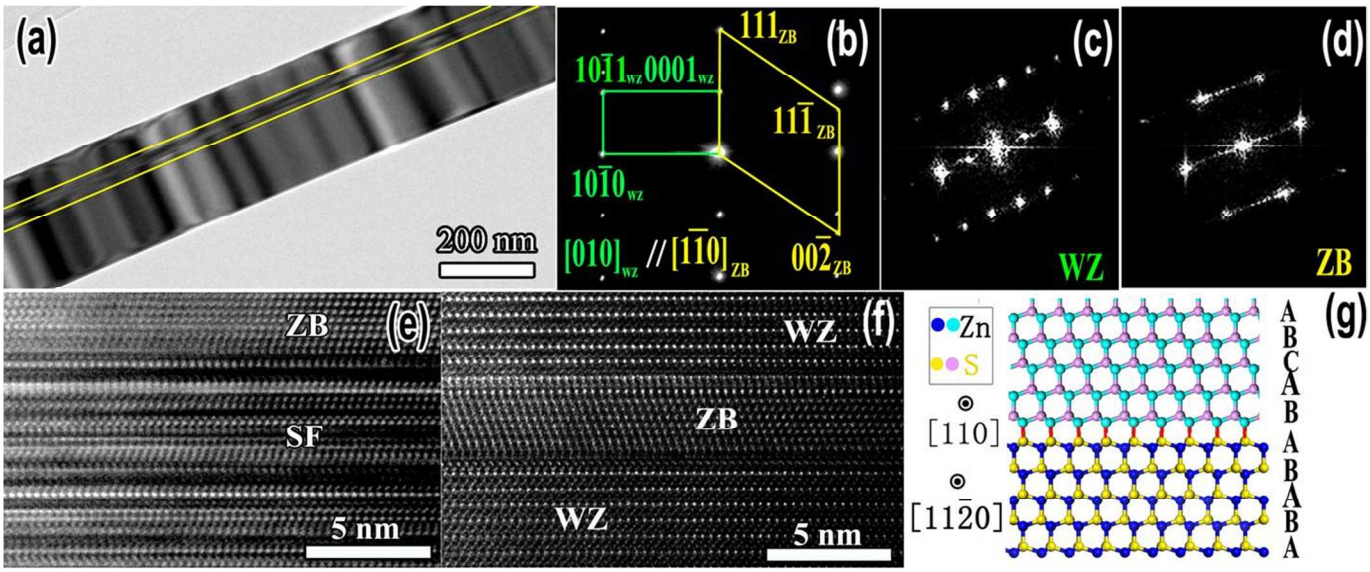

Figure 4 (a) TEM image of a ZnS nanobelt with a narrow strip of defect area; (b) SAED pattern recorded from the strip area. Two separated SAED patterns correspond to WZ-ZnS (green) and ZB-ZnS (yellow), respectively; (c, d) FFT patterns from WZ-ZnS and ZB-ZnS crystal domains; (e) typical defect area including ZB-ZnS and high-density stacking faults inside an individual ZnS nanobelt; (f) atomically resolved TEM image of WZ-ZnS/ZB-ZnS heterostructure area with sharp interface; (g) atomic structural model of WZ-ZnS/ZB-ZnS heterostructure that reflects the atomic ordering at the interface and the atom stacking sequence in each crystal domain.

area (green curve, area "2") displays rather stronger intensity and an obvious peak shift towards the longer wavelength. The predominant luminescence intensity of point "2" is also in good agreement with the monochromatic CL image (Fig. 2c), in which the strip area shows intense UV luminescence.

The insight on the CL emissions of ZnS nanobelts, i.e., the stronger intensity and obvious red-shift in the local strip area compared with these in the edge areas, together with the previous literature reports, has driven us to elucidate the intrinsic origin that is responsible for such a difference in cathodoluminescence. Structural defect-related, impurity-doping or size-dependent quantum confined effect induced peak-shifts have been observed in a variety of semiconductor nanostructures.[25, 26] In this case, the reason ascribed to quantum-size effect can be undoubtedly excluded due to the large strip width (>20 nm). Generally, the quantum size effect induced peak-shift can be observed when the size of ZnS nanostructure is smaller than its critical Bohr radius (2.5 nm). The possibility of impurity doping that leads to the red-shift of cathodoluminescence also becomes negligible because of its high purity proved by EDS analysis. Therefore, the peak-shift observed at different areas in a single ZnS nanobelt may originate from structural defect. In order to demonstrate our hypothesis, the microstructures and crystallinity of several ZnS nanobelts were carefully examined by high-resolution transmission electron microscope (HRTEM) analysis. Surprisingly, all the ZnS nanobelts studied by TEM exhibit a common characteristic: each ZnS nanobelt independent of its dimension and size contains a narrow strip or more defect areas along the growth direction, as presented in Fig. 4a (yellow lines). The strip widths of these areas are ranged from several nanometers to tens of nanometers (<20 nm). A single ZnS nanobelt with different strips can occasionally be observed. Figure 4b shows the selected area electron diffraction (SAED) pattern recorded from the strip area and one can see that two sets of succinct diffraction spots are presented, as plotted in green and yellow lines. Further crystallographic analysis concluded that these two separated SAED patterns can be indexed to hexagonal wurtzite ZnS (WZ-ZnS, green line) and cubic zinc-blende (ZB-ZnS, yellow line) phases, respectively, with two parallel zone axes along [010] and [1-10] directions. The high-resolution TEM image shown in Figure 4f describes the atom stacking sequences of the strip area, corresponding to the SAED pattern in Figure 4b. ZB-ZnS phase with several atomic layers thickness is neighboured with well-crystallized WZ-ZnS phase and the interface between WZ-ZnS/ZB-ZnS phases is extremely sharp and flat. All the atoms near the crystal boundary have a good lattice-matching, as revealed in the SAED pattern, in which the d-spacing of $(002)_{WZ}$ approaches well to that of $(111)_{ZB}$. In fact, it is very common to form such a WZ/ZB heterostructure in wurtzite-type semiconductor nanostructures due to the disorder of atom stacking sequence.[27] As is known to all, ZB structure prefers an atomic stacking ordering ABCABC, whereas WZ structure features as an atomic stacking sequence ABAB, as schematically illustrated in Figure 4g. The extraction of "C" layer will lead to the transition from ZB structure to WZ structure and results in an atomically flat interface with superior lattice-matching (Figure 4f, 4g). The WZ/ZB interface or boundary can induce a strong asymmetric segregation of intrinsic point defects and leads to a transition of shallow acceptor, as observed in ZnO crystal (e. g., V_{Zn}, O_i, and O_{Zn}) and demonstrated again in ZnO tetrapods that contains WZ and ZB phases.[27, 28] Fast Fourier transform (FFT) from WZ-ZnS and ZB-ZnS crystal domains reveals clear diffraction spots (Figure 4c, 4d), implying the local good crystallinity in ZnS nanobelt. In contrast to the WZ/ZB heterostructure, the strip area of ZnS nanobelt is mainly existed in the form of mixed ZB crystal domains and high density of stacking faults (Figure 4e), incorporated into the host WZ-ZnS lattice. Careful HRTEM analyses performed on smooth edge areas concluded that these parts are well crystallized in WZ-ZnS phase without any stacking faults or twins, the same as WZ-ZnS phase shown in Figure 4f.Therefore, it can be concluded that the red-shift of NBE peak emission is directly originated from these mixed defects (stacking fault/phase boundary) locally formed in the nanobelt.

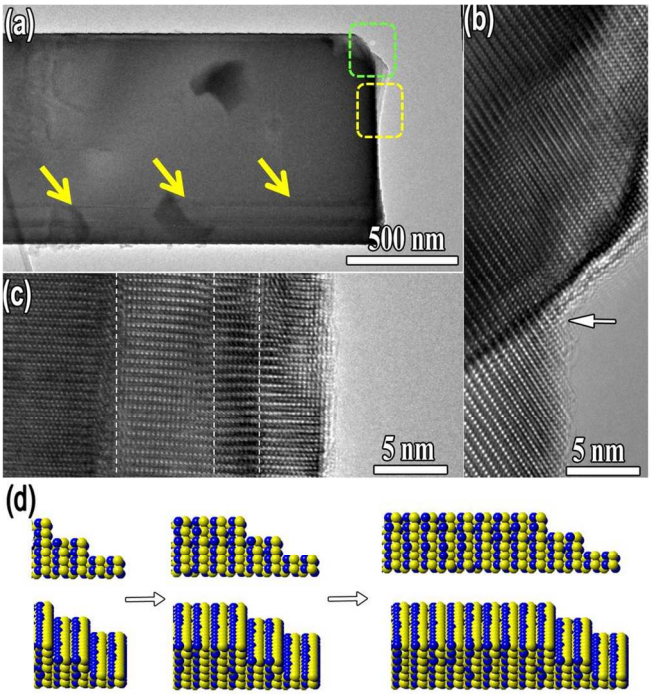

Figure 5 (a) TEM image of a ZnS nanobelt with strips of defect area and terrace-like growth front; (b, c) magnified atomically-resolved TEM images of the tip-end of ZnS nanobelts. Crossing layers and terrace-like atomic steps identified by the layer thickness can be confirmed; (d) atomic structural model that schematically describes the morphology evolution and growth process of one-dimensional nanobelts.

As an additional important finding in this work, the general growth process of nanobelts and their formation mechanism were proposed based on precise TEM observations on ZnS nanobelts. Different from the nucleation and crystallization of cylindric solid nanowires, which have been extensively studied and their formation mechanism has been completely understood, an exact schematic crystalline model describing the general feature of rectangular belt-like nanostructures has rarely been addressed. It is easily understood that nanowires with uniform diameter can be guided by metal catalyst terminated at the tip-end[29] and their diameter is strictly confined by the catalyst size in a vapor-liquid-solid (VLS) process.[30] However, the nucleation process of nanobelts is featured as a completely different behavior with nanowires even though in the case of catalyst existence. Normally, there will be no particles attaching on the tip of nanobelts and thus a vapor-solid (VS) process is mainly responsible for the nanobelt formation, except for triangular nanobelts (or sheets) catalyzed by metal particles.[31] The accurate HRTEM analysis and precise monochromatic CL imaging studies on the defect-containing areas of numerous ZnS nanobelts allow us to further study their tentative formation mechanism. Different from our previous reported ZnS nanostructures (bicrystalline nanobelts,[8] T-shaped ZnS 3D nanoarchitectures[10]), which comprise of high density of twins along the growth direction, ZnS nanobelts synthesized here are always composed of some stacking faults or mixed WZ/ZB phases along axial direction. Figure 5a shows a representative ZnS nanobelt with fixed width and consecutive strip of stacking fault (marked by yellow arrows). One can clearly see the apparent brightness contrast at the tip end and some thinner layers protrude the growth front of ZnS nanobelt. Magnified high-resolution atomic images of the tip-end (marked area with green dash line in Figure 5a) show terrace-like regions with different thicknesses along the growth direction, revealing obvious layered characteristic. The thickness of ZnS nanobelt gradually decreases along the growth front within the investigated area, reflecting the decrease of atomic layer numbers (Figure 5c). Figure 5b depicts the overlapping layers at the end of ZnS nanobelt (yellow dash line in Fig 5a), demonstrating again the crystalline steps. Based on these persuasive evidences, a schematic model describing the crystallization and growth process of belt-like nanostructure was proposed, as shown in Figure 5d. To form belt-like morphology, constituent atoms will first aggregate together to serve as the nucleation terrace via a self-assembled process. It should be mentioned that the initial nucleation plays a key role in dominating the width and thickness of subsequent nanobelt formation during the growth process. Even the defect involved in the belt is closely related to the initial atom disordering arrangement, as demonstrated in HRTEM data (Figure 4). Following the nucleation terrace, which has high surface energy, precursor atoms will repeatedly prefer to deposit on the previously-formed crystalline steps, leading to the local 'epitaxial' and preferential growth, as schematically illustrated in Figure 5d, and finally evolving into belt-like structure. The understanding of ZnS nanobelts formation will help us to further control their morphology, dimension and crystallinity, and explore their potential applications in optoelectronic nanodevices.

Conclusion:

In summary, ZnS nanobelts containing strips of defect along growth direction have been synthesized via a simple sublimation of ZnS powders at 1100 °C. The long and narrow defect areas with a width of tens of nm are comprised of typical stacking faults or mixed ZB-ZnS phase. CL measurements using accurate spatially-resolved spectroscopy and monochromatic contrast maps verified the obvious defect-induced red-shift of NBE peak in the local nanoscaled defect zone (~tens of nm). In addition, the formation mechanism and crystallization process of belt-like nanostructures have been systemically addressed based on precise observation on the growth front of ZnS nanobelt using high-resolution TEM and it is concluded that the initial nucleation terrace plays a key role in dominating the later growth of nanobelts. All these findings will further help us to understand the nucleation, defect engineering and property tailoring of semiconductor nanostructures with promising applications in optoelectronic nanodevices.

Notes and references

[a] Shenyang National Laboratory for Materials Science, Institute of Metal Research (IMR), Chinese Academy of Sciences (CAS), No. 72 Wenhua Road, Shenyang 110016 China. Email: baodanliu@imr.ac.cn; xjiang@imr.ac.cn;
[b]World Premier International (WPI) Center for Materials Nanoarchitectonics (MANA), National Institute for Materials Science (NIMS), Namiki 1–1, Tsukuba, Ibaraki, 305–0044 Japan

Acknowledgement:
B. D. Liu would like to thank the Knowledge Innovation Program of Institute of Metal Research (IMR), Chinese Academy of Science (CAS) (grant No. Y2NCA111A1) for the financial support of this work.

Electronic Supplementary Information (ESI) available: [details of any supplementary information available should be included here]. See DOI: 10.1039/c000000x/

1. X. S. Fang, Y. Bando, M. Y. Liao, U. K. Gautam, C. Y. Zhi, B. Dierre, B. D. Liu, T. Y. Zhai, T. Sekiguchi, Y. Koide and D. Golberg, *Adv Mater*, 2009, **21**, 2034-2039.
2. Z. G. Chen, L. N. Cheng, H. Y. Xu, J. Z. Liu, J. Zou, T. Sekiguchi, G. Q. Lu and H. M. Cheng, *Adv Mater*, 2010, **22**, 2376-2380.
3. B. D. Liu, Y. Bando, X. Jiang, C. Li, X. S. Fang, H. B. Zeng, T. Terao, C. C. Tang, M. Mitome and D. Golberg, *Nanotechnology*, 2010, **21**, -.
4. X. S. Fang, Y. Bando, G. Z. Shen, C. H. Ye, U. K. Gautam, P. M. F. J. Costa, C. Y. Zhi, C. C. Tang and D. Golberg, *Adv Mater*, 2007, **19**, 2593-+.
5. L. Xu, H. W. Song, T. Zhang, H. T. Fan, L. B. Fan, Y. Wang, B. A. Dong and X. Bai, *J Nanosci Nanotechno*, 2011, **11**, 2121-2125.
6. X. F. Wang, H. T. Huang, B. Liang, Z. Liu, D. Chen and G. Z. Shen, *Crit Rev Solid State*, 2013, **38**, 57-90.
7. X. Fang, T. Zhai, U. K. Gautam, L. Li, L. Wu, Y. Bando and D. Golberg, *Prog Mater Sci*, 2011, **56**, 175-287.
8. B. D. Liu, Y. Bando, M. Y. Liao, C. C. Tang, M. Mitome and D. Golberg, *Cryst Growth Des*, 2009, **9**, 2790-2793.
9. W. Liu, N. Wang, R. M. Wang, S. Kumar, G. S. Duesberg, H. Z. Zhang and K. Sun, *Nano Lett*, 2011, **11**, 2983-2988.
10. B. D. Liu, Y. Bando, Z. E. Wang, C. Y. Li, M. Gao, M. Mitome, X. Jiang and D. Golberg, *Cryst Growth Des*, 2010, **10**, 4143-4147.
11. B. D. Liu, Y. Bando, B. Dierre, T. Sekiguchi, C. C. Tang, M. Mitome, A. M. Wu, X. Jiang and D. Golberg, *Nanotechnology*, 2009, **20**, -.
12. T. K. Tran, W. Park, W. Tong, M. M. Kyi, B. K. Wagner and C. J. Summers, *J Appl Phys*, 1997, **81**, 2803-2809.
13. H. C. Ong and R. P. H. Chang, *Appl Phys Lett*, 2001, **79**, 3612-3614.
14. Z. G. Chen, J. Zou, G. Liu, X. D. Yao, F. Li, X. L. Yuan, T. Sekiguchi, G. Q. Lu and H. M. Cheng, *Adv Funct Mater*, 2008, **18**, 3063-3069.
15. G. Z. Shen, Y. Bando, J. Q. Hu and D. Golberg, *Appl Phys Lett*, 2007, **90**.
16. T. Y. Zhai, Z. J. Gu, H. B. Fu, Y. Ma and J. N. Yao, *Cryst Growth Des*, 2007, **7**, 1388-1392.
17. B. Liu, L. Hu, C. Tang, L. Liu, S. Li, J. Qi and Y. Liu, *Journal of Luminescence*, 2011, **131**, 1095-1099.
18. T. Mitsui, N. Yamamoto, T. Tadokoro and S. Ohta, *J Appl Phys*, 1996, **80**, 6972-6979.
19. C. H. Ye, X. S. Fang, M. Wang and L. D. Zhang, *J Appl Phys*, 2006, **99**.
20. H. Liu, L. F. Hu, K. Watanabe, X. H. Hu, B. Dierre, B. Kim, T. Sekiguchi and X. S. Fang, *Adv Funct Mater*, 2013, **23**, 3701-3709.
21. Y. W. Wang, L. D. Zhang, C. H. Liang, G. Z. Wang and X. S. Peng, *Chem Phys Lett*, 2002, **357**, 314-318.
22. Q. Li and C. R. Wang, *Appl Phys Lett*, 2003, **83**, 359-361.
23. J. Lin, B. Dierre, Y. Huang, Y. Bando, C. C. Tang, T. Sekiguchi and D. Golberg, *Nanoscale*, 2011, **3**, 598-602.
24. J. Lin, Y. Huang, J. Mi, X. Zhang, Z. Lu, X. Xu, Y. Fan, J. Zou and C. Tang, *Nanotechnology*, 2013, **24**, 405701.
25. R. Lopez, L. Feldman and R. Haglund, *Phys Rev Lett*, 2004, **93**.
26. I. Moreels, K. Lambert, D. Smeets, D. De Muynck, T. Nollet, J. C. Martins, F. Vanhaecke, A. Vantomme, C. Delerue, G. Allan and Z. Hens, *Acs Nano*, 2009, **3**, 3023-3030.
27. L. Lazzarini, G. Salviati, F. Fabbri, M. Z. Zha, D. Calestani, A. Zappettini, T. Sekiguchi and B. Dierre, *Acs Nano*, 2009, **3**, 3158-3164.
28. M. Schirra, R. Schneider, A. Reiser, G. M. Prinz, M. Feneberg, J. Biskupek, U. Kaiser, C. E. Krill, R. Sauer and K. Thonke, *Physica B*, 2007, **401**, 362-365.
29. B. D. Liu, Y. Bando, L. Z. Liu, J. J. Zhao, M. Masanori, X. Jiang and D. Golberg, *Nano Lett*, 2013, **13**, 85-90.
30. R. S. Wagner and W. C. Ellis, *Jom-J Met*, 1964, **16**, 761-&.
31. T. Hu, B. Liu, F. Yuan, Z. Wang, N. Huang, G. Zhang, B. Dierre, N. Hirosaki, T. Sekiguchi, Y. Bando, D. Golberg and X. Jiang, *J Nanosci Nanotechno*, 2013, **13**, 5744-5749.